Infrared excess and molecular clouds: A comparison of new surveys of far-Infrared and H I 21-cm emission at high galactic latitudes

William T. Reach

Institut d'Astrophysique Spatiale, Université Paris Sud, F–91405 Orsay cedex, France and

Infrared Processing and Analysis Center, California Institute of Technology, MS 100-22,
Pasadena, CA 91125

William F. Wall

Instituto Nacional de Astrofisica, Optica, y Electonica, A. Postal 51 y 216, Puebla, Puebla, Mexico

and

Nils Odegard

Raytheon STX Corporation, 4400 Forbes Blvd., Lanham MD 20706

Received	<u>;</u> accepted

ABSTRACT

We have created a map of the large-scale infrared surface brightness in excess of that associated with the atomic interstellar medium, using region-by-region correlations between the far-infrared and 21-cm line surface brightness. Our study updates and extends a previous attempt with the Infrared Astronomical Satellite and Berkeley/Parkes H I surveys. The far-infrared observations used here are from the Cosmic Background Explorer Diffuse Infrared Background Experiment, which extends far-infrared wavelength coverage to 240 μ m, so that we are reliably sampling the emission of large, thermal-equilibrium grains that dominate the dust mass. The H I data are from the combined Leiden-Dwingeloo and Parkes 21-cm line surveys. Using the maps of excess infrared emission at 100, 140, and 240 μ m, we created an atlas and identified the coherent structures. These infrared excess clouds can be caused both by dust that is warmer than average, or by dust associated with gas other than the atomic interstellar medium. We find very few warm clouds, such as the H II region around the high-latitude B-type star α Vir. The majority of the infrared excess clouds are colder than the average atomic interstellar medium. These clouds are peaks of column density, and their excess infrared emission is due to dust associated with molecular gas. We identify essentially all known high-latitude molecular clouds in the infrared excess maps, and further identify a sample of new clouds with similar infrared properties. The infrared excess was correlated with CO line brightness, allowing us to measure the ratio of H₂ column density to CO line integral (i.e. the $N(H_2)/W(CO)$ conversion factor) for high-latitude clouds. The atlas of infrared excess clouds may be useful as a guide to regions of relatively higher interstellar column density, which might cause high extinction toward extragalactic objects at optical and ultraviolet wavelengths and confusion toward

structures in the cosmic background at infrared and microwave frequencies.

Subject headings: cosmology: diffuse radiation — infrared: ISM: continuum —

ISM: clouds — ISM: molecules

1. Introduction

It has been known for some time that interstellar molecular gas exists away from the galactic midplane, based on the presence of absorption lines of H_2 and other molecules in the spectra of high-latitude stars (Savage et al. 1977) and the presence of millimeter-wave emission of CO from regions of high optical extinction (Blitz, Magnani, & Mundy 1984). However, the pervasiveness of the molecular component of the local interstellar medium has not been convincingly assessed, because of the difficulties of observing molecular gas over large areas. Absorption line observations are restricted either to trace elements or to lines of sight toward the few hot, bright stars at high latitude, because the electronic ground-state transitions of both atomic and molecular hydrogen are in the ultraviolet. Millimeter-wave observations of CO are restricted to relatively small areas because all-sky observations are at present prohibitively expensive. An early survey of randomly-selected lines of sight found a surface filling fraction of 0.5% for $CO(1 \rightarrow 0)$ emission (Magnani, Lada, & Blitz 1986). A large—but, necessarily, incompletely-sampled—survey was recently performed with a very low detection rate of 0.3%, suggesting that the northern galactic hemisphere is largely 'devoid' of molecular gas (Hartmann, Magnani, & Thaddeus 1997). On the other hand, there remains the question of whether a survey in a particular observable quantity, such as the brightness of collisionally-excited rotational line emission of a particular molecule, is really tracing all of the molecular gas. The H₂ and CO might have somewhat different spatial distributions due to their different photodissociation cross-sections and chemistry, and the rotational energy levels of CO may not be excited in low-density $(n(H_2) < 10^3)$ cm^{-3}) environments.

With the advent of the infrared all-sky survey by the *Infrared Astronomical Satellite* (*IRAS*), a new light was cast on study of the interstellar medium (Neugebauer et al. 1984, Low et al. 1984). The 100 μ m surface brightness was found to be well-correlated

with the H I column density on both small and large scales (Boulanger and Pérault 1988), demonstrating its value as a tracer of interstellar gas. If the infrared emission arises from both the atomic and molecular phases of the interstellar medium, then regions with an excess infrared emission relative to the H I column density are likely locations of molecular gas. This effect has been demonstrated in Ursa Major (de Vries et al. 1987) and for isolated cirrus clouds (Heiles, Reach, & Koo 1988; Reach, Koo, & Heiles 1994); in both cases the infrared excess was found to be associated with CO emission. Because the infrared surface brightness and H I column density are known over the entire sky, it is possible to use the difference between the infrared map and an appropriately-scaled map of H I column density to produce an all-sky survey of molecular gas. This idea has been exploited by Désert et al. (1988), who used the IRAS 100 μ m data and the Berkeley H I survey (Heiles and Habing 1974) to create a catalog of infrared excess clouds.

In the present paper, we study the distribution and nature of infrared excess clouds using relatively recent data from the Cosmic Background Explorer¹ (COBE) mission (Boggess et al. 1992) and the Leiden-Dwingeloo H I survey (Hartmann and Burton 1997). These new surveys provide higher sensitivity and higher reliability than the previous infrared and H I observations for large-scale emission. More importantly, the COBE observations at 100, 140 and 240 μ m wavelength are a reliable measure of the emission from large, thermal-equilibrium grains that dominate the dust mass. From a detailed study of the infrared emission in the Orion region, it was shown that the 100, 140, and 240 μ m

¹ The National Aeronautics and Space Administration/ Goddard Space Flight Center (NASA/GSFC) is responsible for the design, development, and operation of the Cosmic Background Explorer (*COBE*). Scientific guidance is provided by the *COBE* Science Working Group. GSFC is also responsible for the development of the analysis software and for the production of the mission data sets.

emission sample essentially the same dust temperature along the line of sight (Wall et al. 1996). Our first results (Reach et al. 1994), based on comparing the COBE 240 μ m optical depth to the Berkeley H I surveys, encouraged us to pursue a more thorough comparison of the H I and infrared data.

The large-scale distribution of molecular gas is important for a number of practical applications.

Extinction of extragalactic objects— Extragalactic observations at visible and shorter wavelengths are affected by extinction even at high galactic latitude. In order to estimate the extinction, which affects both the brightness and color of extragalactic objects, it has been necessary to rely on 21-cm line surveys (cf. Burstein and Heiles 1978). If an extragalactic object lies behind a high-latitude molecular cloud, its extinction will be significantly underestimated using the 21-cm line surveys. The results derived here will help observers to identify regions where anomalously high extinction from molecular clouds can be expected. A recent effort by another group (Schlegel, Finkbeiner, & Davis 1997) systematically addresses this issue, using the COBE and IRAS data to create a map of the extinction. Large-scale variations in the temperature and gas-to-dust ratio were calibrated by Schlegel et al. in a manner very similar to ours. By calculating the column density using large-scale average dust temperature, it is likely that the Schlegel et al. dust maps will underestimate the extinction toward relatively cold clouds such as the molecular clouds we have identified. We therefore recommend that the Schlegel et al. maps be used to estimate the extinction, and that our molecular cloud atlas be used as a supplement, warning of cold, high-extinction clouds. Lines of sight behind these clouds should certainly be avoided unless 1-3 magnitudes (A_V) of extinction can be tolerated.

Shadowing of distant X-rays— Interstellar clouds produce distinct shadows on the soft X-ray emission from the Galactic halo and the extragalactic emission (McCammon and

Sanders 1990). These shadows have been compared to 21-cm line maps and to IRAS 100 μ m surface brightness maps (Snowden, McCammon, & Verter 1993; Wang and Yu 1995). In both cases, the interstellar column density is underestimated in the presence of molecular clouds, because molecular gas can absorb X-rays and molecular clouds are relatively faint at 100 μ m (and nearly invisible at 60 μ m; Laureijs et al. 1996), compared to atomic gas. We provide both a map of infrared excess clouds and a calibration of their column density in the present paper.

Diffuse γ -ray emission and the $N(H_2)/W(CO)$ factor— A significant source of the γ -ray surface brightness of the sky is due to interaction of cosmic rays with interstellar gas. The expected near-linear proportionality of γ -rays with total column density allows a calibration of the molecular column density, when correlated with H I and CO maps (Strong et al. 1988; Digel et al. 1996). In the presence of H₂ clouds with relatively little CO emission, this calibration can be significantly biased. Here we calibrate the molecular column density using the infrared excess, and compare the results to γ -ray studies. The ratio of H₂ column density to CO line integral is important for assessing the vertical mass distribution of molecular gas in the disk of our Galaxy.

Relation to external galaxies— Low-metallicity galaxies such as the Large and Small Magellanic clouds contain relatively fewer giant molecular clouds, and more translucent regions—due to the lack of dust. High-latitude molecular clouds such as studied here share empirical similarities with low-metallicity galaxies, and should provide insight into the nature of the latter.

2. The Correlation of Far-Infrared Emission with H I

2.1. Observations

The far-infrared data used in this work originate from the Diffuse Infrared Background Experiment (DIRBE, Hauser et al. 1997). The DIRBE produced a redundantly sampled all-sky survey in 10 wavebands from the near to far-infrared; here we concentrate on the 100 μ m, 140 μ m, and 240 μ m wavebands, which are dominated by the emission from interstellar dust. In particular, these wavebands are dominated by the emission from the larger grains, in thermal equilibrium with the interstellar radiation field, that dominate the mass of dust in the interstellar medium. Nonetheless, a significant source of large-scale emission, even in the far-infrared, is from the zodiacal light. For this work, we use data from which a model for the zodiacal light has been subtracted (Reach et al. 1996; Kelsall et al. 1998). To minimize detector noise, which is significant for the 140 μ m and 240 μ m wavebands, we use the average of the zodiacal-light-subtracted weekly maps over the cold mission (44 weeks). The instantaneous beamsize of DIRBE is 42'. In order to avoid confusion between the interstellar clouds that we hope to study and bright infrared point sources, we use data from which all pixels containing bright and apparently unresolved structure, as well as circular regions around the Magellanic clouds, have been masked (Arendt et al. 1998). Furthermore, we will not consider here the portion of the sky close to the galactic plane $(|b| < 20^{\circ})$, where clouds from a wide range of distances overlap on the sky. The DIRBE data are gridded into a sky-cube projection, which we degraded to a pixel size of 39' so that each pixel is nearly independent. We assume that the point-to-point uncertainty in the infrared surface brightness at (100, 140, 240 μ m) is a quadrature combination of (0.15, 1.3, 0.75 MJy sr⁻¹) and 2% of the surface brightness, to account for detector noise, pixelization uncertainties, source confusion, and gain drifts. These uncertainty estimates were determined from inspection of the data. At 140 and 240 μ m the point-to-point uncertainty is comparable to the expected instrument noise (cf. Hauser et al. 1998), but at 100 μ m it is significantly larger, so we must have included some of the detected small-scale

sky structure of the interstellar medium. The uncertainties are important in the present work mostly for weighting the data, but they do scale the χ^2 statistics.

The H I 21-cm line data used in this work originate from the Leiden-Dwingeloo survey of the Northern sky (Hartmann and Burton 1997) and the Parkes survey of the Southern sky (Cleary et al. 1979). The Dwingeloo 25-m telescope has a main beam size of 36', which is well-matched to the DIRBE beamsize. An important aspect of the Leiden-Dwingeloo survey is the removal of stray radiation, which is up to half of the observed signal at high galactic latitudes. The near and far sidelobes of the telescope response were mapped using bright point sources, then the sidelobe emission was estimated by convolving the sky map with the beam (Hartmann et al. 1996). For this work we use the integrated 21-cm line brightness, converted into H I column density assuming the emission is optically thin. This latter assumption is unlikely to be violated at high galactic latitude unless the H I gas is colder than 20 K. Gas this cold must be well-shielded from the interstellar radiation field, or else photoelectric heating will raise its temperature to at least 50 K at typical interstellar pressure. In such cold, shielded regions, the H is rapidly converted into H₂, so that the H I column density becomes a negligible fraction of the total. We integrated the H I line over the range of -100 to +100 km s⁻¹, which includes the bulk of local interstellar gas but excludes high-velocity clouds. The high-velocity clouds have been shown to be deficient in interstellar dust (Wakker and Boulanger 1986); therefore they can be ignored in the present study. For declinations south of -30° , we used the 21-cm survey performed with the Parkes 64-m telescope (Cleary et al. 1979). The Parkes survey provides critical information on the southern sky, but it does suffer from undersampling (every beamwidth in right ascension but every other beamwidth in declination) and incompleteness (some survey scans missing). Furthermore, the Parkes survey has not been corrected for stray radiation. We checked the calibration of the Parkes and Leiden-Dwingeloo surveys by comparing their column densities where the surveys overlap; the calibrations were in good agreement. We

assume the point-to-point uncertainty in the H I column density is a quadrature sum of 1×10^{19} cm⁻² and 2% of the column density, to account both for uncertainties in the stray radiation and the gain. The uncertainties were not rigorously determined; they are based on the estimated gain and stray radiation accuracy (Hartmann and Burton 1997).

2.2. Region-by-region correlations

EDITOR: PLACE FIGURE 1 HERE.

In order to identify molecular clouds in the infrared maps, we must first remove the infrared emission from dust associated with the atomic interstellar medium. We presume the column density of the atomic interstellar medium is linearly traced by the integrated 21-cm line brightness. The infrared emission, however, is not a linear tracer of the interstellar dust because it is sensitive to the dust temperature. We considered two methods to calibrate the dust temperature variations: (1) calculate the column density at each pixel using the 100, 140, and 240 μ m brightness ratios assuming a single dust temperature along the line of sight, and (2) calculate the ratio of infrared to H I surface brightness from region to region on the sky. The first method is simpler and, in principle, it could detect temperature changes on angular scales as fine as 1°. But in practice the 140 and 240 μ m maps are very noisy and the 100 μ m map suffers from large-angular-scale zodiacal light residuals (and all wavelengths contain some cosmic infrared background radiation). Furthermore, we show below that the dust associated with molecular gas is significantly colder than that associated with atomic gas, so that a single dust temperature does not apply to the lines of sight we are most interested in. Therefore we used method (2), by dividing the sky into 'cells', with 10° radius, on a regular grid every 10°. Within each cell, we measured the slope and intercept of the pixel-to-pixel infrared surface brightness as a function of H I column

density. To illustrate the procedure, Figure 1 shows an example. In the upper panel, we show the 240 μ m surface brightness versus H I column density for the entire dynamic range of both quantities, within the region 15° in radius centered on galactic coordinates $(l,b)=(140^{\circ},35^{\circ})$. At low H I column densities, there is a linear rise of infrared surface brightness with H I column densities, while at higher column densities there is a wide dispersion. This dispersion is due to infrared emission associated with gas other than H I. At low column densities, interstellar H remains atomic, but where the column density is large, the H becomes molecular. For a uniform-density cloud, the H₂ column density is predicted to exceed the H I column density when

$$N({\rm H~I}) > 2.5 \times 10^{20} \left(\frac{n}{100 {\rm cm}^{-3}}\right)^{-2} \left(\frac{T}{80 {\rm K}}\right)^{-1} {\rm cm}^{-2}$$
 (1)

(Reach et al. 1994). In low-density regions, H₂ cannot form, while in denser clouds such as account for the 21-cm absorption features in front of radio sources (see review by Kulkarni and Heiles 1988), the gas readily forms molecules at column densities $> 3 \times 10^{20} \ \mathrm{cm}^{-2}$. Figure 1 shows this effect: the points at higher H I column densities deviate systematically upward from the straight line fitted to the lower column-density points. This upward deviation, presumably due to infrared emission from dust associated with molecular gas, is what we will call the 'infrared excess.' We presume that on large scales, the warm and cold phases of the interstellar atomic gas exist in pressure equilibrium, and the cold clouds have a relatively small filling factor, so that all lines of sight cross warm regions and some (or all) cross cold regions. In order to exclude cold clouds with column densities sufficient to form H_2 from our infrared-H I correlations—which are intended to measure the properties of the atomic medium only— we exclude all points with a column density more than $3 \times 10^{20} \ \mathrm{cm^{-2}}$ above the minimum column density for the 'cell.' The minimum column density is presumed to represent the warm H I, and by allowing a different threshold in each cell we allow for the longer path length through the warm gas Galaxy at low latitudes. The threshold column density for the Ursa Major/Ursa Minor/Camelopardalis region is shown

as a vertical dashed line in Figure 1.

EDITOR: PLACE TABLE 1 HERE.

For the low-column density pixels within a given sky 'cell,' we perform a linear fit of infrared surface brightness versus H I column density, taking into account the uncertainties in both quantities. For the sample cell, the points used in the fit and their uncertainties are shown in the lower panel of Figure 1. Even at low column densities, there are some outlying positive points, but in no case do the fits appear to be biased by outliers. The resulting slope and intercept for two sample cells, widely separated on the sky, are shown in Table 1. In both cases the fits are 'good' in the sense that the reduced χ^2_{ν} is essentially unity (to within our understanding of the measurement uncertainties). At 240 μ m, the infrared-H I slopes of the two cells are similar, but at 100 μ m the slopes are significantly different. Using the ratio of slopes at 100 and 240 μ m, (and assuming the interstellar dust emissivity varies as ν^2 ; Draine and Lee 1984), we find that the temperature of the dust associated with H I is 17.2 ± 0.2 K in the cell centered on $(140^{\circ}, 35^{\circ})$, and 19.0 ± 0.3 K in the cell centered on (40°, 35°). Even though a 2 K temperature difference between the two cells may seem unimportant, a change in temperature from 17 to 19 K increases the emission at 100 μ m by a factor of 2.4 and the 240 μ m emissivity by a factor of 1.7, so that the ratio of 100/240 μ m emission increases by 60%. The ratio of dust optical depth at 100 μ m (assuming ν^2 emissivity) to gas column density in the two cells are 6.4 and 4.6, respectively, in units of 10^{-25} cm². The absolute calibration uncertainty is $\pm 15\%$ in these dust-to-gas ratios, but the uncertainty in cell-to-cell variations is much less. Therefore, the (30%) difference between the dust-to-gas ratios in these cells is statistically significant.

EDITOR: PLACE FIGURE 2 HERE.

We have calibrated the differences in the dust temperature and dust-to-gas ratio from region to region by performing independent fits of the infrared surface brightness as a function of H I column density at each wavelength and in each sky cell. These fit parameters were well-constrained for most of the sky, but there were some regions where the infrared emission was relatively poorly-correlated with the H I, even at low column densities. If a molecular cloud complex or dust hot-spot is comparable to or larger than our cell size (10°), then it is not possible to calibrate the infrared-H I slope. These regions are generally near the galactic plane, and for the most part they can be identified with well-known star-forming complexes. For each of these complexes, a detailed study using higher-resolution maps is needed to sort out the variations in gas phase and dust heating due to embedded stars (e.g. Boulanger et al. 1998 for the Chameleon complex).

All-sky maps of the infrared-H I slope and offset at 100 μ m are shown in Figure 2. In cells where the fits were found to be poor, we interpolated using adjacent cells. In cells where the fit is good, we interpolated to a finer, 37′ grid in order to avoid discontinuities at cell boundaries. Two regions that stand out in the infrared-H I slope are at $(300^{\circ}, +50^{\circ})$ and $(90^{\circ}, -40^{\circ})$. The former is due to the effect of the nearby, early-type star Spica, whose situation at high latitudes allows it to heat dust over a very large apparent area (Reynolds 85), while the latter is due to the MBM 53/54/55 complex of molecular clouds (Magnani et al. 1985). Our cell size was chosen so that regions like these would not completely disappear once the infrared emission associated with H I is subtracted. In addition to these relatively compact regions, there are real variations in the 100 micron-HI slope due to temperature variations from place to place of the interstellar dust associated with atomic gas. These variations appear in Fig. 2 as large-scale structures. One noticeable problem is at southern declinations, where the H I data from the Parkes survey was used. The infrared emission per H atom is lower there than average, which could be due in part to stray radiation effects in the Parkes survey.

2.3. Implications for the far-infrared background

EDITOR: PLACE FIGURE 3 HERE.

EDITOR: PLACE FIGURE 4 HERE.

For each of the far-infrared wavelengths we have considered here, we find that a positive residual sky brightness remains after subtracting the infrared emission correlated with the H I column densities. Histograms of all the zero-intercepts of the infrared-H I correlation for out grid of sky cells are shown in Fig. 4; it is clear that the zero-intercept is consistently positive. This same result has also been found from the correlations of infrared brightness with H I column density in the Lockman Hole and around the North Ecliptic Pole (Arendt et al. 1998), and for the entire low-column-density portion of the northern sky (Boulanger et al. 1996). At least part of the residual emission is related to the Solar System, because one can see the distinctive pattern of the ecliptic plane in Fig. 2. However, the amplitude of the residual zodiacal light, based on its ecliptic latitude dependence, is small. Furthermore, the spectrum is inconsistent with the zodiacal light, being relatively bright at $240 \mu m$, which argues against a Solar System origin (Dwek et al. 1998). The far-infrared emission remaining after the subtraction of the emission from interstellar dust could be the extragalactic background due to unresolved galaxies, with obvious cosmological significance; alternatively, it could be due to a component of our galaxy with infrared emission but little atomic gas. We will address the cosmological issue only briefly here, as it is the primary focus of other recent papers (Puget et al. 1996; Hauser et al. 1998). In the present work, we have allowed for the possibility that the infrared emission per unit H I column density varies from place to place. In the presence of uncertainties in both variables, the slope and zero-intercept of a correlation tend to be correlated. Because the H I column density is

always positive, the slope and intercept are negatively correlated; furthermore, the intercept is biased toward positive values where the correlation is weak. Comparing the slope and offset of all of the sky cells with a significant fit, we find a near-perfect anti-correlation. This could potentially lead to a false detection of the cosmological background, especially if, at low column densities, the interstellar dust is associated with an interstellar medium other than atomic gas.

EDITOR: PLACE TABLE 2 HERE.

The infrared emission per unit H I column density has a well-defined mean value, with few regions of abnormally high or low values. Table 2 lists the mean and rms dispersion of the infrared emission per unit H I column density and the zero-intercept of the infrared-H I correlation at 100, 140, and 240 μ m. It is clear that the range of slopes and intercepts obtained over the high-latitude sky is significantly larger than the uncertainty of an individual value, so that the range of slopes is not due to random measurement or fitting uncertainties. The wavelength-dependence of the slopes in the two sample regions (Tab. 1) indicates that this is mostly a dust temperature effect. This is a gradual, large-scale effect, that is not confined to the few outstanding cells. The cells with an infrared-H I slope more than 1.5 times the rms away from the mean are shaded in Fig. 3 and Fig. 4. It is evident that the outlying regions in terms of infrared-H I slope are also outlying in terms of the zero-intercept (as expected because of the anti-correlation of slope and intercept mentioned above). Over the entire sky, there is a significant, positive sky brightness that cannot be explained by interstellar dust associated with H I. If the range of slopes shown in Fig. 3 is a real effect due to the interstellar medium, then the range of offsets in Fig. 4 is also due to the Galaxy. The inferred brightness of an isotropic extragalactic background must then be lower than the *lowest* offset value. In principle, variations in the infrared-H I correlation on scales smaller than those chosen for the present work could lead to an even wider range of

slopes and offsets. The dispersion of the putative infrared background brightnesses, listed in the last column of Table 2 precludes more than a '2- σ ' (loosely speaking) confidence level detection of the infrared background, unless more restrictive assumptions about the galactic emission are made. The significance of this effect is discussed in more detail by Hauser et al. (1998) and Shafer et al. (1998). Fortunately, the separation of the galactic and cosmological contributions to the far-infrared sky brightness can be resolved using higher-resolution and sensitivity far-infrared observations, such as have recently been performed with the Infrared Space Observatory (Kawara et al. 1997, Puget et al. 1998) and will eventually become possible with the NASA Space Infrared Telescope Facility and the ESA Planck Surveyor. These observations should reveal whether the brightness of the faintest parts of the sky is produced by an ensemble of extragalactic sources or by interstellar cirrus.

3. The Distribution of Infrared Excess

3.1. Definition of infrared excess

The infrared excess is defined to be the observed infrared surface brightness minus the contributions from dust associated with the atomic interstellar medium, the zodiacal light, and the cosmic infrared background. We calculate the infrared excess using

$$I_{\nu}^{ex} = I_{\nu} - S * N(H I) - O,$$
 (2)

where S and O are the locally-interpolated slope and offset of the infrared-H I correlation. The offset O contains residual zodiacal light and the cosmic infrared background, and is not useful for measuring properties of the interstellar medium. We created infrared excess maps independently for the 100, 140, and 240 μ m wavebands, so that we can measure the far-infrared colors of the infrared excess. The infrared excess map at 240 μ m is shown in an all-sky projection in Figure 5. The infrared excess is 'patchy,' with significant structure

-17 -

on scales smaller than the size of the 'cells' within which the infrared-H I slopes were

determined. We have checked that the maps are not very different if the cell size is twice

as large as the one we finally adopted. The significance of a given value of the infrared

excess can be determined statistically from its probability distribution. Figure 6 superposes

the histograms of the positive and negative pixels in the infrared excess map. It is clear

that the probability distribution is not random, and that the *positive* values significantly

outnumber the negative values when $I_{100}^{ex} > 0.3 \text{ MJy sr}^{-1}$, which we will use as the lower

limit to define infrared excess clouds.

EDITOR: PLACE FIGURE 5 HERE.

EDITOR: PLACE FIGURE 6 HERE.

3.2. Atlas of infrared excess clouds

A table of clouds would not suffice to describe the infrared excess, because the emission

has some continuity over large scales. High-latitude molecular clouds have been shown

to be associated with large H I features (Gir, Blitz, & Magnani 1994), suggesting their

formation is related to events or processes (like supernovae and stellar winds) that organize

the interstellar medium on large scales. For presentation here, and practical utility to

other researchers, we present the infrared excess as an atlas consisting of 8 maps with

simple coordinate projections. We have preferred a Cartesian projection for latitudes

 $20^{\circ} < |b| < 50^{\circ}$, so that positions can be easily located with a ruler (Fig. 7). We also made

maps of the two galactic polar caps, in a simple orthographic projection (Fig. 8). The

maps we present here are for 100 μ m wavelength, the highest-sensitivity of the DIRBE

far-infrared wavebands. The maps at 140 and 240 μ m are generally similar. At 100 μ m, there are more infrared excess clouds, because both warmer-than-average and molecular clouds produce infrared excess at 100 μ m. However, the vast majority of structures in the far-infrared excess maps are shown in the next sections to be *cold*.

EDITOR: PLACE FIGURE 7 HERE.

EDITOR: PLACE FIGURE 8 HERE.

In order to study the properties of the 'clouds' and regions of sky with infrared excess, we have identified two lists of positions and apertures within which to perform photometry. The first list is the catalog of previously-known molecular clouds compiled by Magnani, Hartmann, & Speck (1997). (We combined entries that would be redundant at our low resolution.) These are indicated on the individual panels of the atlas. Second, we made a list of some of the remaining peaks in the infrared excess maps, with brightness comparable to the known molecular clouds. This list was created by hand, upon inspection of both 100 μ m and 240 μ m infrared excess maps, and it is incomplete. The 'new' clouds were named in the format $DIR_{ll} \pm bb$ where lll is the galactic longitude and bb is the galactic latitude; the prefix 'DIR' stands for 'diffuse infrared' as in the name DIRBE. Third, for reference, we labeled many peaks in the infrared excess maps due to bright point sources, most of which are nearby galaxies (Odenwald, Newmark, & Smoot 1997). The list of previously-known clouds is shown in Table 3, and the newly-identified clouds are shown in Table 4. For each cloud, we averaged the infrared excess surface brightness at 100 and 240 μ m within the cloud boundary. Only clouds detectable both at 100 μ m and 240 μ m are listed. The total infrared excess flux at 100 μ m, the color temperature obtained from the 100/240 μ m ratio (assuming emissivity proportional to ν^2), and the angular diameter of each cloud is shown in Tables 3 and 4.

EDITOR: PLACE TABLE 3 HERE.

EDITOR: PLACE TABLE 4 HERE.

The infrared excess clouds in general are relatively bright at 240 μ m, and their far-infrared color temperature is significantly lower than that of average atomic clouds. This is illustrated in Figure 10, where histograms of the color temperatures of infrared clouds are shown. The fact that the vast majority of infrared excess clouds are cold confirms that the infrared excess is generally not due to clouds that are warmer than average. Indeed, because the clouds are colder than average, they tend to be under-luminous in infrared emission. This effect has also been found by Lagache et al. (1997), who showed that molecular regions at high latitude can be identified by (1) deficiency in 60 μ m emission and (2) low 140/240 μ m color temperatures relative to atomic cirrus. One of the main uncertainties that has been faced by past studies of infrared excess as a tracer of molecular gas (e.g. Désert et al. 1988; Reach et al. 1994) was the uncertainty as to whether the infrared surface brightness at 60 μ m, observed by IRAS and often compared to the 100 μ m brightness, traces variations in column density or dust temperature. Using the COBE observations at 240 μ m, this problem has now been resolved.

3.3. Warm infrared excess clouds

While they are rare, there are some infrared excess clouds that are warmer than average. The single most prominent example is the large H II region around the nearby B star α Vir, or Spica, which was first discovered by its extensive H α emission (Reynolds 85). The Spica H II region is exceptional, in that it is produced by one of the closest—at $d = 80 \pm 5$ pc (ESA 1997)—early-type stars; it is at high galactic latitude, where it can be

easily separated from other sources; and the star is presently in a region of relatively low interstellar medium density, so that its H II region covers a region some 15° across. The dust in the Spica H II region is significantly warmer than typical interstellar cirrus, and it is unusual in that it also has 12 and 25 μ m emission significantly higher than expected from the 100–240 μ m emission, suggesting a modified grain size distribution (Zagury 1997). There are no other 'warm' infrared excess clouds comparable to the Spica H II region in size and brightness, most likely because no other early-type star is as advantageously situated.

One significant 'warm' infrared excess cloud that has not been noted before is DIR015+54. This is one of the brightest 100 μ m infrared excess clouds at high positive galactic latitudes (Fig. 8a), but it is not detected at 240 μm (and therefore is absent from Table 4). In order to see the structure of this cloud at higher angular resolution, we extracted IRAS images at 12, 25, 60, and 100 μ m from the IRAS Sky Survey Atlas (ISSA). The cloud is relatively bright at 60 μ m, with a local-background-subtracted surface brightness, averaged over the central 30', of 0.8 MJy sr⁻¹. The ratio of 60/100 μm brightnesses is 0.46, a factor of 2 higher than that of atomic 'cirrus' and much higher than that of molecular clouds. The ISSA 60 μ m image is shown in Figure 9. The cloud is structured in a form qualitatively suggestive of a bow-shock produced by an object moving toward the northeast. Bow-shocks were discovered in the IRAS data due to the stand-off between the interstellar medium and the stellar winds of early-type stars with significant transverse velocities (van Buren and McCray 1988), and their morphologies and 60/100 μ m colors are comparable to the cloud shown in Figure 9. However, there is no early-type star in the vicinity that could plausibly create this nebula, either as an H II region or a bow shock. Such a star would be very bright at visible and ultraviolet wavelengths, owing to the low extinction along the line of sight and the proximity needed to heat a region of such a large angular size. There is a peak of 60 μ m emission approximately at the location where a wind-source would be located. The nature of this emission peak, listed in the IRAS

Faint Source Catalog as F15101+1206 (Moshir et al. 1989), is presently unknown, though statistically it is likely to be extragalactic (Reach, Heiles, & Koo 1993). Apart from some of the peaks in the nebula, which appear in the IRAS Faint Source Catalog, nearby there are only some galaxies and stars of type A and later in the SIMBAD database. We find that there is a faint optical counterpart of F15101+1206 in the Palomar Observatory Sky Survey², consistent with the idea that F15101+1206 is extragalactic. There is no optical counterpart for the diffuse emission of DIR015+54. The infrared colors of DIR015+54 are similar to those of the nearby galaxy NGC 6822 (Israel et al. 1996), suggesting perhaps that the cloud could in fact be another low surface brightness member of the Local Group. We inspected the individual H I spectra from the Leiden-Dwingeloo 21-cm line survey near this position, and we find that the cloud is clearly present, with a 'normal' LSR velocity of -17 km s⁻¹ and both narrow and wide line components (dispersions 3 and 15 km s⁻¹, respectively). We suspect therefore that DIR015+54 is a Galactic cloud that happens to be somewhat brighter than average in the far-infrared, and much brighter than average at 60 μ m. The nature of this cloud and the other large, 'warm' clouds in the COBE/DIRBE and IRAS data remains mysterious. They are either locally-heated regions or regions with unusual grain size distributions, but we do not know why; this should be investigated further.

²Based on photographic data of the National Geographic Society – Palomar Observatory Sky Survey (NGS-POSS) obtained using the Oschin Telescope on Palomar Mountain. The NGS-POSS was funded by a grant from the National Geographic Society to the California Institute of Technology. The plates were processed into the present compressed digital form with their permission. The Digitized Sky Survey was produced at the Space Telescope Science Institute under US Government grant NAG W-2166.

3.4. Comparison with known molecular clouds

Our atlas of infrared excess clouds reveals essentially all previously known high-latitude molecular clouds in the literature (Magnani et al. 1996). First, consider the clouds originally found by Magnani, Blitz, & Mundy (1985, hereafter MBM); these clouds were first identified as regions of extinction on the Palomar Observatory Sky Survey plates, and then they were detected in $CO(J=1\to 0)$ emission with radio telescopes. At our low angular resolution, the MBM clouds comprise essentially 36 individual regions. Of these, well-formed clouds with significant infrared excess ($I_{100}^{ex}>1$ MJy sr⁻¹) were clearly detected from 34 regions, for a 94% detection rate. MBM 19 and MBM 9, the two regions for which we do not see an infrared 'cloud', both are in regions of significant infrared excess, but there is no well-defined cloud at their position. Indeed this is somewhat true of some of the other clouds as well: the center of the infrared excess region does not coincide with the center of the MBM cloud. We suspect that the MBM positions are relatively dense cores (with well-defined extinction on the optical plates), while the overall cloud structure is better represented by the infrared excess map.

EDITOR: PLACE FIGURE 10 HERE.

Our atlas of infrared excess is significantly different from the catalog of 515 infrared excess clouds obtained by Désert et al. (1988) [DBB]. We have attempted to associate each entry of Tables 3 and 4 with a cloud in the DBB catalog. For 62 % of the MBM clouds, we find corresponding entries in the DBB catalog. This is somewhat higher than the 47% detection rate determined by DBB, because of the way we grouped MBM clouds into complexes and considered a match if the DBB and MBM positions fall within the same cloud in Figs. 7 or 8. Specifically, this means we consider the MBM clouds to be much larger than the high-extinction and CO-emitting cores. The higher detection rate of MBM

clouds in our atlas is due to the higher quality input data that we used; both infrared and HI are of substantially higher quality than the data available to DBB. Many of the clouds that are not listed in DBB are very bright in our atlas, including both well-known (MBM) and new clouds. On the other hand, a significant fraction of DBB clouds are not confirmed by the present analysis. In total, we find counterparts for 45% of the DBB clouds and hints for another 7%, leaving 48% with no evident infrared excess in our maps. Of the unconfirmed clouds, 58% have a 'significance' criterion less than 5 listed in the DBB table, but 10% (mostly H I artifacts) are listed with 'significance' greater than 7. The uncertainties in the infrared excess method—especially with the lower-quality infrared and H I data used by DBB, but also with the results presented in this paper—are dominated by systematic uncertainties rather than random noise. We have therefore chosen to make a relatively short table of 81 selected clouds, and to present the sky maps for use by others.

EDITOR: PLACE FIGURE 11 HERE.

The interstellar medium is not an ensemble of clouds with well-defined boundaries—it is coherent over large angular scales. Therefore a comparison of cloud catalogs can be misleading. There are few regions where the $CO(J=1\to 0)$ line has been mapped in emission on scales large enough to make a meaningful comparison with our atlas. The largest-scale high-latitude CO map of which we are aware was made with a 1.2-m telescope, whose large beam (9') is well-suited to comparison with our results. A large portion of the Ursa Minor-Ursa Major region has been covered in a number of surveys, including one very large, regularly sampled grid (Heithausen et al. 1993). We have projected our infrared excess map onto the grid of the CO map assembled by Heithausen et al. (1993) for detailed comparison—see Figure 11. The agreement between the contour of integrated CO line brightness, W(CO), and the infrared excess contour is remarkably good, and the infrared excess map contains no significant clouds in regions without CO. Figure 12

shows a pixel-by-pixel scatter diagram for these maps. A linear fit, taking into account the statistical uncertainties of 0.5 K km s⁻¹ in W(CO) and 0.3 MJy sr⁻¹ in I_{100}^{ex} yields the following:

$$W(CO) = (-0.19 \pm 0.05) + (1.17 \pm 0.05) \left(I_{100}^{ex}/\text{MJy sr}^{-1}\right) \text{ K km s}^{-1},$$
 (3)

where only statistical uncertainties were accounted for. The correlation of 100 μ m emission with H I column density in this region (which largely overlaps with that shown in Fig. 1) yields

$$I_{100} = 0.47 \pm 0.1 + (0.62 \pm 0.03) \left(N(\text{H I}) / 10^{20} \text{ cm}^{-2} \right) \text{ MJy sr}^{-1}.$$
 (4)

If the infrared emission per H nucleus were the same in atomic and molecular gas, then we find that the H₂ column density per unit integrated $CO(1 \rightarrow 0)$ line brightness is

$$N(\rm H_2)/W(\rm CO) = (0.7 \pm 0.1) \times 10^{20} \, \rm cm^{-2} \, K^{-1} \, km^{-1} \, s.$$
 (5)

If they were sufficiently orthogonal, we could determine the separate emissivities of the atomic and molecular gas using a multiple linear regression between the infrared, H I, and CO surface maps over the parts of the region that have been observed at all three wavelengths. Table 5 shows the slopes from fits of the form

$$I_{\nu} = aN(\text{H I}) + bW(\text{CO}) + c \tag{6}$$

for several infrared wavelengths. It is evident that a and b depend on wavelength differently, and the interpretation is straightforward: the dust mixed with the atomic gas has a different temperature from the dust mixed with the molecular gas. The color temperature inferred for the dust mixed with the atomic gas is $T_1 = 17.0 \pm 0.3$ K, and for the dust mixed with the molecular gas it is $T_2 = 14.7 \pm 0.2$ K. The observation that atomic and molecular clouds have different infrared spectra implies that their relative column densities cannot be simply determined using observations at a single wavelength. This has an important practical

implication. Naïvely, the ratio

$$X_{naive} = 0.5b/a \tag{7}$$

gives the column density of H_2 per unit CO line integral; values of X_{naive} are listed in the last column of Table 5. It is evident that the naïvely inferred value of X changes by a factor of 2 depending on the wavelength, which is inconsistent with the idea that the infrared emission is a linear tracer of the total column density. We can, however, calibrate this effect using the results obtained here. We assume that within the molecular phase, the gas is completely molecular and the dust-to-gas ratio is the same as in the atomic phase. Then the column density of H_2 per unit CO line integral is

$$X = \frac{1}{2} \frac{b}{a} \frac{B_{\nu}(T_1)}{B_{\nu}(T_2)},\tag{8}$$

(Magnani and Onello 1995) which results in the last column of Table 5. When calibrated this way, a self-consistent description of the infrared emission from the atomic and molecular phases could be obtained from observations at a single wavelength—if the temperature contrast between the atomic and molecular components were the same everywhere. Clearly, observations at 240 μ m are the best infrared tracer of molecular gas, because the 240 μ m emission is less sensitive to temperature changes.

The H₂ column density per unit CO line integrated intensity has been measured by several techniques and for several different regions, with a fairly wide range of results. The 'canonical' method is to correlate γ -ray emission—due to interaction of cosmic rays with nuclei—with the CO and H I emission simultaneously. This correlation has been performed in the galactic plane, where the CO emission is dominated by giant molecular clouds, and $X = (2.3 \pm 0.3)$ has been found ³ (Strong et al. 1988). The correlation of γ -ray emission and CO line brightness in the Ursa Major/Ursa Minor region yielded $X = (0.92 \pm 0.1)$

 $^{^3{\}rm Units}$ for X throughout this paper are $10^{20}~{\rm cm}^{-2}~[{\rm K~km~s}^{-1}]^{-1}.$

(Digel et al. 1996). The γ -ray method, like the 'naïve' infrared method, assumes that the γ -ray emission properties of the atomic and molecular clouds are the same. In fact, recent observations of lower-energy γ -rays indicate that the value of X inferred depends on the energy of the γ -rays, with values ranging from (1.1–4) (Strong et al. 1994). If the difference is due to processes that only operate at low energies, then the 'canonical' value of 2.3 holds, for it was determined at high energies; however, until this is understood, there remains the possibility that even the 'canonical' X is uncertain by a factor of 2.

The infrared method of locating and estimating the column density of H_2 is especially useful because a wide range of physically different types of cloud can be observed. For the galactic center, Sodroski et al. (1995) found that the value of X is an order of magnitude lower than in the outer Galaxy. Their analysis takes into account the higher dust temperature in the galactic center, because they used the dust optical depth from 140 and 240 μ m observations. At high latitudes, the molecular clouds are smaller, so one might anticipate a difference in the H_2 column density per unit CO line integrated intensity due to the higher radiation fields that can penetrate a smaller cloud. An analysis very similar to our multiple linear regression was performed for the Ursa Major clouds using higher-angular-resolution 21-cm line observations with the Effelsberg 100-m telescope and IRAS 100 μ m data (de Vries et al. 1987). Their infrared map clearly revealed the presence of the clouds that were not evident in the 21-cm line map, and the combined H I and CO maps were found to reproduce the infrared brightness, with $X_{naive} = (0.5 \pm 0.3)$. Using the temperature of atomic and molecular clouds we found for the entire North Celestial Pole region,

$$X = 3.8X_{naive} = (1.9 \pm 1.1) \times 10^{20} \,\mathrm{cm}^{-2} \,[\mathrm{K \ km \ s}^{-1}]^{-1}.$$
 (9)

The corrected X for the Ursa Major clouds is consistent with the 'canonically' adopted γ -ray results.

For some clouds, however, the H₂ column density per unit CO line integral is significantly different from canonical values. The cloud HRK236+39 was observed in the 21-cm line with the Arecibo 305-m telescope, which provides the highest-resolution single-dish observations of an isolated, diffuse interstellar cloud (Reach et al. 1994). For this cloud, the linear regression of the H I, CO, and infrared maps resulted in the 'naïvely' determined value $X_{naive} = (0.16 \pm 0.03)$. This low value is not due to a temperature effect: we find in the present work that the color temperature of the far-infrared excess emission is 16.5 K, only slightly colder than that of atomic gas. In order to explain the low X_{naive} with a temperature difference alone, the temperature of the molecular gas would have to be 13.2 K. While this might seem similar to the observed 16.5 K, it is in fact clearly ruled out: for the same 100 μ m brightness, the 240 μ m emission of the cloud would be more than 4 times brighter than observed. For HRK236+39, comparison of the H I, CO, and infrared maps clearly shows that there is a component of the infrared emission that is not traced by H I 21-cm or $CO(1 \rightarrow 0)$ line emission. The infrared excess exists in the central $\sim 45'$ of the cloud, while the CO is concentrated even more to the center, in clumps with size $\sim 2'$. Similar results have been found from a comparison of infrared and CO maps of the Chameleon region by Boulanger et al. (1997). They found that the large clouds, with extensive CO emission, $X_{naive} = (0.6-1.0)$, which could easily be explained by a somewhat lower dust temperature in the molecular clouds. The large scatter in the comparison of CO and extinction maps—which are independent of the dust temperature—was found to be due to spatially coherent regions where the gas is primarily H_2 but the CO abundance is low.

EDITOR: PLACE TABLE 5 HERE.

Any map of molecular gas, even over a very restricted region, would allow us to calibrate the infrared excess. Where it has been observed, the extinction of background starlight provides a temperature-independent tracer of the total column density. Comparison of

extinction and CO maps for high-latitude clouds yields X = (0.4-6.4) (Heithausen & Thaddeus 1990; Magnani, Blitz, & Wouterloot 1988), but it is unclear whether the large scatter is due to real cloud-to-cloud variations or calibration difficulties in the extinction maps (which are obviously uncertain when the extinction is appreciably more than unity). The H₂ molecule is symmetric, so that its rotational transitions must be quadrupolar, and the lowest-energy transition has an energy of 500 K, which cannot be excited under typical interstellar conditions. Absorption line studies are able to trace cold, diffuse gas, but the paucity of suitable background stars makes comparison to large-beam observations problematic. A promising method is to observe the low-energy radio transitions of the CH molecule, because CH forms readily—but only where the H is molecular. Magnani & Onello (1995) have observed a set of both translucent and dark molecular clouds in the 9-cm lines of CH, and used the empirical correlation of CH line brightness with extinction to obtain the H_2 column density. They find that X = (0.3-6.8) for translucent high-latitude clouds: a substantial range, as was found from the extinction studies. The value of X was also found to vary within clouds, where it was observed for more than one position. A detailed comparison of our results with those of Magnani & Onello (1995) is complicated by the fact that the clouds are structured on scales smaller than our beam, while the CH lines have not been mapped over the clouds. While there is clearly an infrared excess counterpart of each of the clouds in their sample, only 11 lines of sight are suitable for comparison; we find that the ratio of 240 μm infrared excess to H₂ column density (inferred from the CH line brightness) ranges from 0.4 to $2 \text{ MJy sr}^{-1}/(10^{20} \text{ cm}^{-2})$. It is unclear whether the range of values is due to beam size effects or a true variation from cloud to cloud, but this comparison at least affords a calibration of the infrared excess independent of CO. For comparison, the calibration of 240 μ m emission per H₂ for the North Celestial Pole region yields

$$I_{\nu}(240 \,\mu\text{m})/N(\text{H}_2) = b/X = 1.0 \pm 0.2 \text{ MJy sr}^{-1} (10^{20} \,\text{cm}^{-2})^{-1}$$
 (10)

using Table 5, which is within the range given by the CH calibration.

EDITOR: PLACE FIGURE 12 HERE.

4. Conclusions

The infrared excess clouds, which were found after removing emission associated with the atomic interstellar medium, are predominantly molecular clouds. The dust in these clouds is colder than dust in diffuse atomic clouds, for the same reason that the gas is molecular: the outer layers of the cloud shield the center from the dust-heating and molecule-dissociating effects of the interstellar radiation field. These molecular clouds fill only a small fraction of the high-latitude sky. The column density of the infrared excess clouds can be estimated using the calibrations discussed above, which may be rewritten as

$$I_{100}^{ex}/N(\mathrm{H}_2) = (0.26 \pm 0.05) \times 10^{-20} \,\mathrm{cm}^2 \mathrm{MJy \, sr}^{-1}.$$
 (11)

We can estimate the mass surface density of the infrared excess clouds, using the difference between positive and negative excess for $|b| > 20^{\circ}$ (Fig. 6). The surface density is about $0.3~M_{\odot}~{\rm pc^{-2}}$ (including 40% He by mass), roughly equally partitioned among regions of low and high brightness. (We adjusted for the part of the sky at $|b| < 20^{\circ}$ by assuming it has the same average infrared excess as the rest of the sky.) The mass density that we find is an order of magnitude larger than that found in an unbiased, wide-field CO survey (Hartmann et al. 1998) of the northern sky, but it is comparable to a previous estimate—also based on CO—of the total mass of the known molecular clouds at high galactic latitude (Magnani et al. 1996). We suspect that the unbiased survey missed much of the molecular gas because either there was no CO mixed with the diffuse H₂ or the CO rotational levels were subthermally excited (because of low H₂ volume density). We do *not* find a great

disparity between the northern and southern galactic hemispheres (cf. Hartmann et al. 1998); according to the infrared excess, the southern galactic hemisphere has about 30% more molecular gas than the northern hemisphere. The high-latitude infrared-excess clouds comprise a significant fraction of the total mass of molecular gas in the solar neighborhood.

The infrared excess maps can be used to provide a guide to regions of anomalously high extinction. The extinction calculated from the H I column density (cf. Burstein and Heiles 1978) can significantly underestimate the total extinction in these regions. If we assume that the dust in the infrared-excess clouds has the same extinction cross-section per H-nucleus as diffuse clouds for which this quantity has been measured (Bohlin, Savage, & Drake 1978), then the extinction due to infrared excess clouds can be obtained from Fig. 7, after multiplying the 100 μ m surface brightness by $A_V/I_{100}^{ex} \sim 0.027$ mag MJy⁻¹ sr.

WTR was supported by NASA's *COBE* project during the early part of this work, through a contract to the Universities Space Research Association. In searching for counterparts for the objects found in this work, we use the *SkyView* facility at NASA Goddard Space Flight Center; *SkyView* is supported by NASA ADP grant NAS 5-32068. We also made use of the SIMBAD database, which is maintained by the Centre de Donnees astronomiques de Strasbourg (CDS), France. We thank Xavier Désert, François Boulanger, Rick Arendt, Janet Weiland, Tom Sodroski, and Mike Hauser for their comments and suggestions.

REFERENCES

- Arendt, R. G. et al. 1998, ApJ, submitted
- Benjamin, R. A., Venn, K. A., Hiltgen, D. D., & Sneden, C. 1996, ApJ, 464, 836
- Blitz, L., Magnani, L., & Mundy, L. 1984, ApJL, 282, L9
- Boggess, N. W., Mather, J. C., Weiss, R., Bennett, C. L., Cheng, E. S., Dwek, E., Gulkis,
 S., Hauser, M. G., Janssen, M. A., Kelsall, T., Meyer, S. S., Moseley, S. H., Murdock,
 T. L., Shafer, R. A., Silverberg, R. F., Smoot, G. F., Wilkinson, D. T. and E. L.
 Wright 1992, ApJ, 397, 420
- Bohlin, R. C., Savage, B. D., & Drake, J. F. 1978, ApJ, 224, 132
- Boulanger, F., & Pérault, M. 1988, ApJ, 330, 964
- Boulanger, F., Bronfman, L., Dame, T. M., & Thaddeus, P. 1998, A&A, 332, 273
- Boulanger, F., Abergel, A., Bernard, J.-P., Burton, W. B., Désert, F.-X., Hartmann, D., Lagache, G., Puget, J.-L. 1996, A& A, 312, 256
- Burstein, D., & Heiles, C. 1978, ApJ, 225, 40
- Cleary, M. N., Heiles, C., & Haslam, C. G. T. 1979, A& AS, 36, 95
- Désert, F. X., Bazell, D., & Boulanger, F. 1988, ApJ, 334, 815
- Désert, F. X., Boulanger, F., & Puget, J.-L. 1990, A& A, 327, 215
- de Vries, H. W., Thaddeus, P., & Heithausen, A. 1987, ApJ, 319, 723
- Digel, S. W., Grenier, I. A., Heithausen, A., Hunter, S. D., & Thaddeus, P. 1996, ApJ, 463, 609

- Draine, B. T., & Lee, H. M. 1985, ApJ, 285, 89
- Dwek, E., Arendt, R. G., Hauser, M. G., Fixsen, D., Kelsall, T., Leisawitz, D., Pei, Y. C., Wright, E. L., Mather, J. C., Moseley, S. H., Odegard, N., Shafer, R., Silverberg, R. F., & Weiland, J. L. 1998, ApJ, submitted
- ESA 1997, The Hipparcos and Tycho Catalogues, ESA SP-1200
- Gir, B.-Y., Blitz, L., & Magnani, L. 1994, ApJ, 434, 162
- Hartley, M., Tritton, S. B., Manchester, R. N., Smith, R. M., & Goss, W. M. 1986, A& AS, 63, 27
- Hartmann, D., & Burton, W. B. 1997, Atlas of Galactic Neutral Hydrogen (Cambridge University Press: Cambridge)
- Hartmann, D., Kalberla, P. M. W., Burton, W. B., & Mebold, U. 1996, A& AS, 312, 256
- Hartmann, D., Magnani, L., & Thaddeus, P. 1998, ApJ, 492, 205
- Hauser, M. G., Kelsall, T., Leisawitz, D., & Weiland, J. L., eds., COBE Diffuse Infrared Background Experiment Explanatory Supplement, version 2.1, COBE reference publication #97-A (Greenbelt: NASA/GSFC), available in electronic form from the National Space Science Data Center
- Hauser, M. G., Arendt. R. G., Kelsall, T., Dwek, E., Odegard, N., Weiland, J. L., Freudenreich, H. T., Reach, W. T., Silverberg, R. F., Moseley, S. H., Pei, Y. C., Mather, J. C., Smoot, G. F., Wilkinson, D. T., & Wright, E. L. 1998, ApJ, submitted
- Heiles, C., & Habing, H. J. 1974, A& AS, 14, 1
- Heiles, C., Reach, W. T., & Koo, B.-C. 1988, ApJ, 332, 313 (HRK)

- Heithausen, A., & Thaddeus, P. 1990, ApJL, 353, L49
- Heithausen, A., Stacy, J. G., de Vries, H. W., Mebold, U., & Thaddeus, P. 1993, A& A, 268, 265
- IRAS Point Source Catalog, Version 2, 1988, Joint IRAS Science Working Group (Washington, DC: GPO)
- Israel, F. P., Bontekoe, T. R., & Kester, D. J. M. 1996, A& A,308, 723
- Kawara, K., Taniguchi, Y., Sato, Y., Okuda, H., Matsumoto, T., Sofue, Y., Wakamatsu,
 K., Matsuhara, H., Hasegawa, T., Chambers, K. C., Cowie, L. L., Joseph, R. D.,
 Sanders, D. B., & Wynn-Williams, C. G. 1997, in *Diffuse Infrared Radiation and the IRTS*, eds. H. Okuda, T. Matsumoto, & T. Rollig (San Francisco: ASP), p. 386
- Kelsall, T., Weiland, J. L., Franz, B. A., Reach, W. T., Arendt, R. G., Dwek, E., Freudenreich, H. T., Hauser, M. G., Moseley, S. H., Odegard, N. P., & Silverberg, R. F. 1998, ApJ, submitted
- Keto, E. R., & Myers, P. C. 1986, ApJ, 304, 466
- Kulkarni, S. R., & Heiles, C. 1988, in *Galactic and Extragalactic Radio Astronomy: Second Edition*, ed. G. L. Verschuur and K. I. Kellermann (Berlin: Springer-Verlag), 95
- Lagache, G., Abergel, A., Boulanger, F., & Puget, J.-L. 1998, A& A, in press
- Laureijs, R. J., Haikala, L., Burgdorf, M., Clark, F. O., Liljeström, T., Mattila, K., & Prusti, T. 1996, A& A 315, L317
- Low, F. J., et al. 1984, ApJL, 278, L19
- Luhman, M. L., & Jaffe, D. 1996, ApJ, 463, 191

Magnani, L., Blitz, L., & Mundy, L. 1985, ApJ, 295, 402 (MBM)

Magnani, L., Blitz, L., & Wouterloot, J. G. A. 1988, ApJ, 295, 402

Magnani, L., Hartmann, D., & Speck, B. G. 1996, ApJS, 106, 447

Magnani, L., Lada, E. A., & Blitz, L. 1986, ApJ, 301, 395

Magnani, L., & Onello, J. S. 1995, ApJ, 443, 169

McCammon, D., & Sanders, W. T. 1990, ARA& A, 28, 657

Moshir, M. et al. 1992, Explanatory Supplement to the IRAS Faint Source Survey, Version 2, JPL, Pasadena

Neugebauer, G., et al. 1984, ApJL, 278, L1

Odenwald, S., Newmark, J., & Smoot, G. 1997, preprint astro-ph/9610238

Puget, J.-L., Abergel, A., Bernard, J. -P., Boulanger, F. Burton, W. B., Désert, F.-X., Hartmann 1996, A& A, 308, 5

Puget, J.-L., Lagache, G., Clements, D., Reach, W. T., Aussel, H., Bouchet, F., Cesarsky, C., Désert, F. X., Elbaz, D., Franceschini, A., & Guiderdoni, B. 1998, in preparation

Reach, W. T., Heiles, C., & Koo, B.-C. 1993, ApJ, 412, 127

Reach, W. T., Koo, B.-C., & Heiles, C. 1994, ApJ, 429, 672

Reach, W. T., Franz, B. A., Kelsall, T., and J. L. Weiland 1996, in *Unveiling the Cosmic Infrared Background*, ed. E. Dwek (New York: AIP), 37

Reach, W. T., Wall, W. F., Hauser, M. G., Sodroski, T. J., Odegard, N., & Weiland, J. L. 1994, BAAS, 185, 57.09

Reynolds, R. J. 1985, AJ, 90, 92

Sargent, W. L. W., Steidel, C. C., & Bocksenberg, A. 1988, ApJS, 68, 439

Savage, B. D., Bohlin, R. C., Drake, J. F., & Budich, W. 1977, ApJ, 216, 291

Schlegel, D. Finkbeiner, D. P., & Davis, M. 1998, ApJ, in press

Shafer, R., et al. 1998, in preparation

Snowden, S. L., McCammon, D., & Verter, F. 1995, ApJL, 309, L21

Sodroski, T. J., Odegard, N., Dwek, E., Hauser, M. G., Freedman, J., Kelsall, T., Wall, W. F., Berriman, G. B., Odenwald, S. F., Bennett, C., Reach, W. T., & Weiland, J. L., 1995, ApJ, 452, 262

Stark, R. 1995, A& A, 301, 873

Strong, A. W., Bennett, K., Bloemen, H., Diehl, R., Hermsen, W., Morris, D., Schoenfelder, V., Stacy, J. G., de Vries, C., Varendorff, M., Winkler, C., Youssefi, G. 1994, A&A, 292, 82

Strong, A. W., et al. 1988, A&A, 207, 1

van Buren, D., & McCray, R. 1988, ApJL, 336, L67

Wakker, B. P., & Boulanger, F. 1986, A& A, 170, 84

Wall, W. F., Reach, W. T., Hauser, M. G., Arendt, R. G., Weiland, J. L., Berriman, G. B., Bennett, C. L., Dwek, E., Leisawitz, D., Mitra, P. M., Odenwald, S. F., Sodroski, T. J., & Toller, G. N. 1996, ApJ, 456, 566

Wang, Q. D., & Yu, K. C. 1995, AJ 109, 698

Zagury, F. 1997, Ph. D. thesis, Université Paris-Sud (Orsay, France)

This manuscript was prepared with the AAS $\mbox{\sc IAT}_{\mbox{\sc E}}\mbox{\sc X}$ macros v4.0.

- Fig. 1.— Infrared surface brightness at 240 μ m observed by DIRBE plotted versus the atomic gas column density from the Leiden-Dwingeloo 21-cm line survey for the Ursa Major/Ursa Minor/Camelopardalis region. In the top panel, nearly the full dynamic range of H I and infrared brightness is shown; 56 points, out of 2393 total, with $N({\rm H~I}) > 1.6 \times 10^{21}~{\rm cm}^{-2}$ were excluded. Error bars are shown for a few points for illustration. The vertical dashed line indicates the threshold column density below which a linear fit was performed. The bottom panel shows the same data, but with restricted dynamic range covering only the points used in the fit, $N({\rm H~I}) < 3.75 \times 10^{20}~{\rm cm}^{-2}$. The linear fit to the low-column density points is shown in both panels as a diagonal solid line. In this paper we concentrate on the positive residuals from the linear fits, which we attribute to dust associated with ionized and molecular gas.
- Fig. 2.— All-sky maps of the slope (a) and offset (b) of the correlation between 100 μ m surface brightness and H I column density. The maps are shown in a galactic-coordinate Mollweide projection with the galactic center at the center. Meridians are drawn every 60°, and parallels are drawn every 30°. The greyscale ranges are labeled to the right of the images; for panel (a) in MJy sr⁻¹ / $(10^{20} \text{ cm}^{-2})$, and for panel (b) in MJy sr⁻¹.
- Fig. 3.— Histograms of the slopes of the infrared-H I correlations for sky patches with 10° radius. Each panel shows the results from a different DIRBE waveband: (a) $100 \mu m$, (b) $140 \mu m$, (c) $240 \mu m$. The 'outlying' values of the slope, defined as being more than 1.5 times the rms away from the mean, are shaded.
- Fig. 4.— Similar to previous figure, but this time for the *offsets* of the infrared-H I correlations for sky patches with 10° radius. Each panel shows the results from a different DIRBE waveband: (a) 100 μ m, (b) 140 μ m, (c) 240 μ m. The sky patches with 'outlying' slope are shaded.

Fig. 5.— All-sky map of the residual 240 μ m surface brightness after subtracting the emission correlated with the H I column density. The map is shown in a galactic-coordinate Mollweide projection as Figure 2; meridians are drawn every 60° and parallels every 30°. The greyscale range is illustrated by the bar, with units MJy sr⁻¹, to the right of the map.

Fig. 6.— Histograms of the infrared excess at 100 μ m. The upper histogram shows the distribution of the positive values of infrared excess, and the curve beneath it shows the distribution of the negative values. The positive values clearly dominate above an infrared excess of 1 MJy sr⁻¹.

Fig. 7.— An atlas of the 100 μ m infrared excess in galactic-coordinate Cartesian projections, for absolute galactic latitudes 20° to 50°. Each map covers 120° of longitude, with the centers at longitudes 0° (a), 120° (b), and 240° (c). The upper part of each page shows positive galactic latitudes, and the lower part shows negative galactic latitudes. In each panel, the most significant clouds are identified and labeled using the catalog of Magnani et al. (1997) or, for new clouds the 'DIRIII±bb' cloud name. The greyscale ranges from -0.2 (white) to 5 (black) MJy sr⁻¹ at 100 μ m wavelength. Contours are drawn at 0.3, 1, 2, 3, and 4 MJy sr⁻¹ (but the highest levels are not present in every map). The large black areas are masked, either because of lack of H I data, presence of the Magellanic clouds, or presence of extremely bright and structured infrared emission.

Fig. 8.— Maps of the 100 μ m infrared excess at the galactic poles, in orthographic projections. Panel (a) covers the north galactic pole and panel (b) covers the south galactic pole. As in the previous figure, the most significant infrared excess clouds are labeled. The greyscale range, from white to black, is -0.2 to 3 MJy sr⁻¹. Contours are drawn at 0.1, 1, 0.5, 1, and 2 MJy sr⁻¹. (The contours are at lower values in this figure than in Figure 7, in order to bring out fainter features near the poles.) The large black stripe in panel (b) is due to a region where the H I 21-cm data are poorly sampled.

Fig. 9.— Surface brightness map at 60 μ m of the warm infrared excess cloud DIR015+54, made from the *IRAS Sky Survey Atlas*. The minimum surface brightness in the map is -1.83 MJy sr⁻¹ (negative because of oversubtraction of zodiacal light), and the contours are at -1.35, -1, and -0.65 MJy sr⁻¹.

Fig. 10.— Histograms of color temperatures of MBM clouds (top) and DIRBE clouds (bottom) obtained from the infrared excess at 100 and 240 μ m. The color temperature of emission associated with the atomic gas is shown as a dashed line. Both the MBM clouds, which are known to be molecular, and the new infrared excess clouds are colder than atomic clouds, most likely because they are optically thick to the high-energy part of the interstellar radiation field.

Fig. 11.— Comparison of the infrared excess (smooth contours) and $CO(1 \rightarrow 0)$ line integral for the Ursa Major-Ursa Minor-Camelopardalis region. Regions where the CO was observed are surrounded by thick lines and filled with thin diagonal lines. The two maps are in very good agreement where data for both maps exist. The infrared excess predicts, accurately, the location and extent of the molecular clouds. Furthermore, there are no 'extra' infrared excess clouds predicted in the regions where CO was observed but not detected.

Fig. 12.— Correlation of the infrared excess, I_{100}^{ex} (MJy sr⁻¹), and CO(1 \rightarrow 0) line integral, W(CO) (K km s⁻¹ for the North Celestial Pole region. Each point corresponds to an independent $40' \times 40'$ pixel.

Table 1. Infrared to H I Correlations for Two Regions (or Cells)

	$(l,b) = (140^{\circ}, 35)$	5°)		$(l,b) = (40^{\circ}, 35^{\circ})$		
Wavelength	Slope	Offset	χ^2_{ν}	Slope	Offset	χ^2_{ν}
	$[{\rm MJy~sr^{-1}}~/~10^{20}~{\rm cm^{-2}}]$	$[{\rm MJy~sr^{-1}}]$		$[{\rm MJy~sr^{-1}}~/~10^{20}~{\rm cm^{-2}}]$	$[{\rm MJy~sr^{-1}}]$	
$100~\mu\mathrm{m}$	0.56 ± 0.01	0.63 ± 0.02	1.25	0.89 ± 0.01	0.33 ± 0.04	1.77
$140~\mu\mathrm{m}$	1.12 ± 0.06	1.01 ± 0.14	1.06	1.45 ± 0.06	0.44 ± 0.21	0.91
$240~\mu\mathrm{m}$	1.02 ± 0.03	0.62 ± 0.08	1.26	1.07 ± 0.04	0.42 ± 0.12	0.91

Table 2. Statistics of Slopes and Intercepts^a

Wavelength	Slope $[{ m MJy~sr^{-1}} \ / \ 10^{20} \ { m cm^{-2}}]$	Offset $[MJy sr^{-1}]$	Offset w/o outliers ^b $[\mathrm{MJy}\ \mathrm{sr}^{-1}]$
100 μ m 140 μ m 240 μ m	0.62 ± 0.08 0.95 ± 0.17 0.72 ± 0.11	0.76 ± 0.37 1.11 ± 0.63 0.87 ± 0.55	0.71 ± 0.32 1.10 ± 0.52 0.83 ± 0.41

 $^{^{\}rm a}{\rm mean}$ and rms dispersion, from cell to cell

 $^{^{\}mathrm{b}}\mathrm{excluding}$ those regions for which the slope deviates by more than 1.5 times its dispersion from its mean value

Table 3. Infrared Excess from Known High-Latitude Molecular Clouds

Name ^a	l	b	size [deg]	$T(240/100)^{\rm b}$ [K]	F_{100}^{ex} ^b [kJy]
DC001.4-21.6	1.4	-21.6	0.6	16.2	1.31
R Cor Bor	4.0	-25.5	2.0	17.1	
LDN 134	5.0	36.0	3.0	14.8	
MBM 45	9.8	-28.0	1.0	14.2	0.72
MBM 39	11.4	36.2	1.9	16.6	1.56
MBM 40	37.6	44.7	2.2	15.9	0.48
MBM $46/48$	40.3	-35.3	2.0	16.9	2.12
HD 210121	57.5	-44.0	4.0	16.3	3.57
G61-34	61.3	-34.0	1.3	15.2	1.16
MBM 49	64.7	-26.8	1.0		
MBM 50	70.0	-30.7	5.5	21.0	1.85
G72 + 25	71.0	25.5	1.0	17.7	
$\mathrm{MBM}\ 51/52$	74.0	-51.3	4.0	17.0	0.66
MBM 55	89.2	-40.9	3.4	14.6	1.77
MBM 41/44	90.0	38.9	1.8	15.7	
MBM 53	93.0	-32.2	4.4	19.0	
MBM 54	93.0	-37.5	4.3	15.9	•••
HRK 94.8+38	94.8	37.5	1.2		
MBM 56	102.7	-28.1	2.5	17.2	1.24
MBM 1	110.2	-41.2	0.5	17.8	0.57
MBM 2	117.7	-52.6	1.9	19.0	1.28
HSVMT 1	119.1	28.5	1.8	15.9	0.61
Polaris	125.0	28.0	5.0	15.1	0.79
HSVMT 12/14	125.5	32.5	1.0	16.0	0.33
MBM 3	130.0	-46.8	2.5	15.4	1.21
MBM 4	134.2	-45.0	2.0	14.7	0.63
HRK 135+51	135.6	51.3	1.5	16.2	0.62
HRK 135-69	136.4	-68.3	1.8	17.9	2.32

Table 3—Continued

$Name^{a}$	l	b	size $[deg]$	$T(240/100)^{b}$ [K]	F_{100}^{ex} [kJy]
HRK 135+54	136.5	54.8	1.1	17.5	2.86
HRK 140+48	140.5	48.0	0.7	24.4	0.74
$\mathrm{MBM}\ 27/29$	142.0	35.0	2.2	15.6	
$\mathrm{MBM}\ 30$	142.2	38.2	3.4	15.2	0.50
Camelopardalis	143.5	24.0	2.9	16.0	0.61
$\mathrm{MBM}\ 5$	145.0	-49.9	3.8	13.8	0.60
MBM 6	147.0	-39.0	1.9	15.0	1.07
$\mathrm{MBM}\ 31/32$	147.0	40.0	4.2	15.9	
MBM 7-8	150.9	-38.3	1.5	14.8	2.87
HSVMT 27	153.6	36.9	2.8	15.7	2.20
G155-40	154.7	-39.8	1.4	15.2	0.91
$\mathrm{MBM}\ 26$	156.4	32.6	2.0	18.1	
$\mathrm{MBM}\ 11/14$	159.0	-33.6	3.5	15.3	0.62
MBM 17	165.7	-25.6	0.5	••••	
MBM 16	171.2	-37.7	0.5	15.5	0.77
$\mathrm{MBM}\ 23/24$	172.0	26.9	0.8	15.5	0.84
MBM 25	173.6	31.2	2.0	15.9	
MBM 19	186.0	-29.9	0.5		
MBM 18	189.1	-36.0	0.5		
MBM 15	191.7	-51.3	3.5	17.7	
HRK 192-67	192.0	-67.5	1.4	18.5	2.29
CB 28	204.0	-25.2	1.5	14.9	0.28
MBM 21-22	208.3	-28.0	2.0	19.6	0.53
G211+63	210.8	63.1	2.0	18.4	
MBM 20	210.9	-36.5	2.5	15.4	2.27
HRK 225-66	227.0	-66.1	2.5	15.6	2.69
HRK 228-29	229.0	-28.5	1.7	16.4	
HRK 236+39	236.0	38.0	4.0	16.5	0.22

Table 3—Continued

Name ^a	l	b	size [deg]	$T(240/100)^{\rm b}$ [K]	F_{100}^{ex} b [kJy]
KM 273+29	272.5	29.7	2.0	17.9	0.65
KM 293-31	291.0	-31.0	2.2		
KM 300-24	301.1	-24.5	2.0		
MBM 33	359.1	36.7	1.2	15.7	

^aCloud names mostly from the compilation of high-latitude molecular clouds (Magnani et al. 1996). MBM: extinction patches on Palomar Observatory Sky Survey (Magnani et al. 1985), KM, DC: extinction patches in European Southern Observatory sky survey (Keto and Myers 1986; Hartley et al. 1986), HRK: infrared cirrus patches in IRAS 100 μ m maps (Heiles et al. 1988)

^bValues listed as '...' in clouds for which the *COBE*/DIRBE data indicates strong, unresolved structure (consistent with a bright point source.)

 ${\bf Table\ 4.}\quad {\bf Catalog\ of\ Unidentified\ Infrared\ Excess\ Clouds}$

Name	l	b	size	T(240/100)	F_{100}^{ex}
			[deg]	[K]	[kJy]
DIR002+31	1.6	-30.8	1.2	18.4	0.89
DIR009+30	9.1	-30.1	2.3	16.5	2.50
DIR013+40	12.8	40.0	1.5	17.1	1.31
DIR018+37	17.8	-36.5	2.5	12.2	0.04
DIR020+45	19.5	-44.5	1.7	18.9	0.69
DIR021+52	21.0	52.0	1.5	17.5	0.29
DIR025+35	25.0	35.0	3.5	21.8	2.96
DIR027+31	26.5	-30.5	1.0	15.3	0.52
DIR028+54	28.3	53.7	1.0	17.3	0.29
DIR029+25	28.5	25.0	2.6	16.6	2.15
DIR029+30	28.5	30.0	1.1	16.7	0.72
DIR034+26	34.0	26.0	3.0	18.6	3.21
DIR046+37	45.5	-36.5	1.6	16.1	1.24
DIR046+33	45.7	-33.0	2.2	22.4	0.72
DIR048+25	47.7	24.5	2.1	16.9	1.49
DIR048+38	48.0	38.0	2.5	18.0	1.56
DIR060+26	59.7	-26.0	1.7	22.3	1.07
DIR061+22	61.0	22.0	4.0	26.1	3.57
DIR070+23	69.7	22.5	1.2	17.2	0.63
DIR071+43	71.0	-42.5	3.0	15.5	3.14
DIR072+34	71.5	-34.0	1.4	15.9	0.43
DIR077+37	76.5	-37.0	3.3	18.5	1.75
DIR081+39	81.3	38.5	2.5	16.2	0.80
DIR087+29	86.5	28.5	3.5	23.1	1.07
DIR096+23	96.2	23.0	2.0	19.3	1.17
DIR098+44	98.0	-44.0	2.5	17.4	0.97
DIR105-31	105.0	-31.0	1.8	15.3	1.16
DIR105-38	105.0	-38.0	2.7	15.7	2.48

Table 4—Continued

Name	l	b	size	T(240/100)	F_{100}^{ex}
			[deg]	[K]	[kJy]
			. 0,	. ,	,
DIR108-27	108.0	27.0	2.7	18.1	2.12
DIR117-44	116.5	-44.0	2.0	18.0	0.70
DIR120-28	120.0	-28.0	2.4	17.7	1.28
DIR121-45	120.9	-45.0	1.8	15.5	0.57
DIR126-37	126.0	37.0	0.9	16.7	0.30
DIR132-30	131.5	-29.5	1.9	18.4	0.61
DIR134-36	134.0	-35.5	1.5	16.3	0.62
DIR135-38	134.5	38.0	1.4	23.4	0.28
DIR135-41	134.7	40.6	1.4	17.0	0.34
DIR140-45	140.0	-44.5	2.0	19.8	0.63
DIR150-29	150.2	-28.5	1.7	16.2	0.89
DIR152-47	152.0	-46.5	3.0	16.2	2.74
DIR164-44	163.5	-44.0	1.6	17.0	0.61
DIR172-42	172.0	-41.5	2.3	15.6	2.87
DIR177-33	177.2	33.0	1.5	16.3	0.56
DIR179-49	179.0	-49.0	3.5	20.4	1.68
DIR184-26	183.5	26.0	1.8	17.8	0.66
DIR187-43	187.0	-42.5	1.7	20.4	0.58
DIR196-24	196.0	24.2	1.0	17.2	0.46
DIR198-32	198.0	32.0	1.5	15.8	0.61
DIR201-24	200.5	23.6	1.3	19.9	0.39
DIR203-32	202.5	-31.5	2.0	14.9	0.33
DIR204-37	203.5	-36.5	1.8	15.6	0.79
DIR216+27	216.3	26.5	2.2	16.2	0.34
DIR223+37	223.0	-37.0	2.7	22.3	1.21
DIR234+37	234.0	-37.0	1.1	21.2	0.65
DIR237+44	237.0	-44.0	1.2	19.7	0.72
DIR239-25	239.0	-25.0	4.0	20.5	3.34

Table 4—Continued

Name	l	b	size	T(240/100)	F_{100}^{ex}
			$[\deg]$	[K]	[kJy]
DIR245+35	245.0	34.8	2.1	17.1	0.88
DIR257 + 34	256.5	34.0	1.5	16.2	0.76
DIR265 + 31	265.0	-30.9	3.0	16.2	1.96
DIR274+46	274.0	-45.8	1.4	18.1	0.63
DIR276 + 33	275.7	33.4	1.2	18.4	0.52
DIR280+55	280.0	-55.0	3.1	17.0	0.91
DIR281-40	280.5	39.5	2.0	23.6	0.48
DIR282+41	282.0	-41.0	4.0	17.6	3.42
DIR288+32	287.5	32.0	3.0	18.5	2.12
DIR289-53	289.0	-53.0	3.5	16.2	0.95
DIR290-62	290.0	-62.0	4.5	18.3	2.20
DIR292-37	292.0	-37.0	3.0	17.7	2.71
DIR310+39	310.0	39.0	1.9	16.8	0.99
DIR313-34	313.0	-34.0	1.5	18.1	0.62
DIR314-47	314.0	-46.5	4.4	19.8	2.76
DIR316+39	316.1	38.5	1.4	18.6	0.61
DIR321+36	321.0	-36.0	2.5	19.2	2.32
DIR327+30	327.0	-30.0	3.0	17.6	2.86
DIR331-34	331.0	-33.5	2.1	21.4	0.69
DIR333+36	333.0	-36.0	1.9	17.0	0.74
DIR335-40	334.5	-40.0	1.3	19.1	0.71
DIR340-43	339.5	-43.3	1.4	16.0	0.50
DIR349-46	348.5	-46.0	1.9	20.1	0.93
DIR354-37	354.0	36.5	1.6	17.8	0.72
DIR357-29	357.0	-29.0	1.3	15.7	0.60

Table 5. Multiple Linear Regression between Infrared, H I, and CO Maps^a

Wavelength	$a = I_{\nu}/N({\rm H~I})$ [MJy sr ⁻¹ / 10 ²⁰ cm ⁻²]	$b = I_{\nu}/W(\text{CO})$ [MJy sr ⁻¹ / (K km s ⁻¹)]	$\chi^2_{ u}$	$X = N(\mathrm{H}_2)$ $[10^{20} \ \mathrm{cm}^{-2}/($,, , ,
				naïve	true
$100~\mu\mathrm{m}$	0.48 ± 0.02	0.34 ± 0.03	1.1	0.35 ± 0.05	1.3 ± 0.3
$140~\mu\mathrm{m}$	1.06 ± 0.08	1.24 ± 0.12	0.8	0.58 ± 0.11	1.5 ± 0.4
$240~\mu\mathrm{m}$	0.94 ± 0.06	1.33 ± 0.10	1.2	0.71 ± 0.11	1.3 ± 0.2

 $^{{\}rm ^aFor}$ the Ursa Major/Ursa Minor/Camelopardalis region

This figure "f1.gif" is available in "gif" format from:

This figure "f2.gif" is available in "gif" format from:

This figure "f3.gif" is available in "gif" format from:

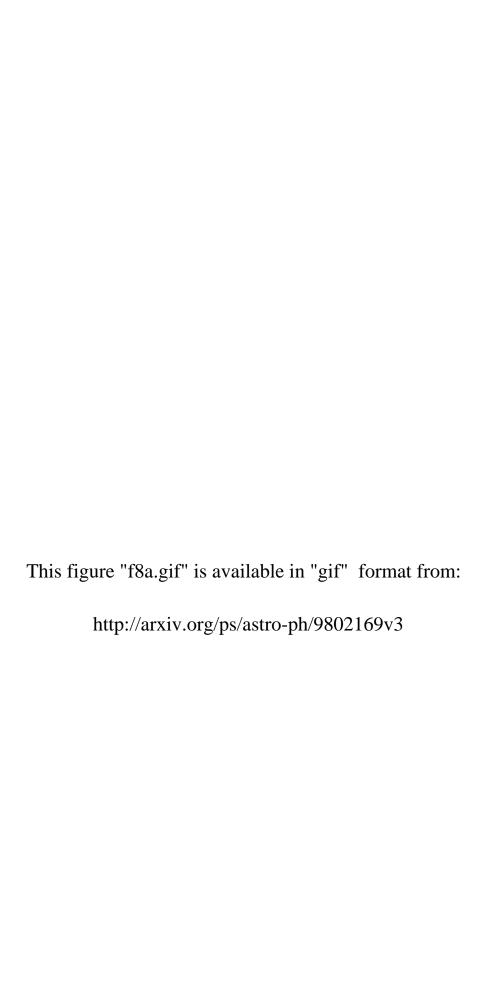
This figure "f4.gif" is available in "gif" format from:

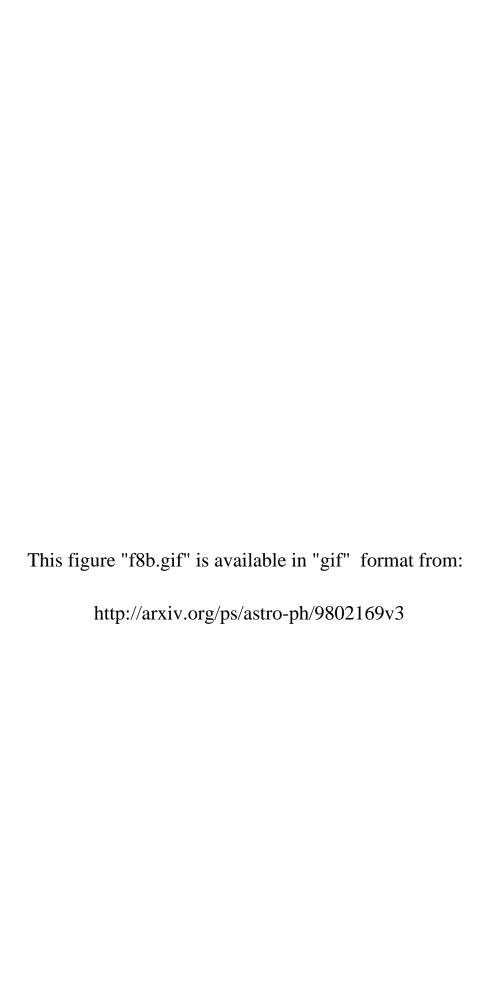
This figure "f5.gif" is available in "gif" format from:



This figure "f7a.gif" is available in "gif" format from: http://arxiv.org/ps/astro-ph/9802169v3 This figure "f7b.gif" is available in "gif" format from: http://arxiv.org/ps/astro-ph/9802169v3

This figure "f7c.gif" is available in "gif" format from:





This figure "f9.gif" is available in "gif" format from:

This figure "f10.gif" is available in "gif" format from:

This figure "f11.gif" is available in "gif" format from:

This figure "f12.gif" is available in "gif" format from: